https://doi.org/10.1016/j.jpowsour.2019.04.065

High-throughput, super-resolution 3D reconstruction of nano-structured solid oxide fuel cell electrodes and quantification of microstructure-property relationships

Yanxiang Zhang,*[a] Fuyao Yan,[a] Mufu Yan,*[a] Yanhong Wan,[b] Zhenjun Jiao,[c] Changrong Xia,[b] Fanglin Chen,[d] Meng Ni[e]

a. National Key Laboratory for Precision Hot Processing of Metals, MIIT Key Laboratory of Advanced Structure-Function Integrated Materials and Green Manufacturing Technology, School of Materials Science and Engineering, Harbin Institute of Technology, Harbin 150001, China.

b. CAS Key Laboratory of Materials for Energy Conversion, Department of Materials Science and Engineering, University of Science and Technology of China, Hefei, 230026, China.

c. College of Science, Harbin Institute of Technology, Shenzhen 518055, China.

d. Department of Mechanical Engineering, University of South Carolina, SC 29205, USA.

e. Building Energy Research Group, Department of Building and Real Estate, The Hong Kong Polytechnic University, Hung Hom, Kowloon, Hong Kong, China.

* E-mail address: hitzhang@hit.edu.cn (Y. Zhang); yanmufu@hit.edu.cn (M. Yan)

Abstract:

Nano-structuring methods are actively applied to solid oxide fuel cell electrodes to reduce the operating temperature while preserving a high electro-catalytic activity. The unique nanoscale microstructure is vital to electrochemical performance, yet not well quantified in three dimensions. Here, with a multi-stage recovering principle of distance correlation functions, the three-dimensional microstructures of $La_{0.8}Sr_{0.2}MnO_{3-\delta}$ nanoparticles infiltrated porous $Y_{0.16}Zr_{0.84}O_{2-\delta}$ electrodes are reconstructed with a dimension of 1024×1024×1024 voxels at a resolution of 7.5 nm from one two-dimensional micrograph. The key geometric characteristics, such as tortuosity factors, active surface/interface areas and three-phase boundary length, are calculated from the reconstructed three-dimensional microstructures at various loadings of $La_{0.8}Sr_{0.2}MnO_{3-\delta}$. Combining with the analysis of distribution of relaxation times, the active three-phase boundary length is shown to be the main factor governing the electrode impedance, and is related quantitatively to the electrochemical process at high frequency. The accuracy of capturing nanoscale features is validated by the focused ion beam sectioning dataset of a Ni-$Y_{0.16}Zr_{0.84}O_{2-\delta}$ electrode at nanoscale resolution. This work provides a promising strategy for reconstructing three-dimensional heterogeneous nanostructures from one super-resolution two-dimensional micrograph, and demonstrates a quantitative approach for uncovering processing-structure-property relationships of nanostructured electrodes and beyond.

Keywords:

Solid oxide fuel cells; Microstructure; Infiltration; Three-dimensional reconstruction

1. Introduction

The performance of solid oxide fuel cells (SOFCs) is dominated by the activities of electrode processes, such as gaseous diffusion in pores, chemical and electrochemical reactions at materials surface, conduction of charged species in bulk materials and charge transfer at interfaces [1]. The electrode processes are strongly affected by the coupled effects of electrochemical properties and three-dimensional (3D) microstructures of electrodes. In the nano-structured electrodes prepared by infiltration [2-6] or exsolution [7-10] of nano-scale (typically 50 nm) catalytic particles for low-temperature and high-performance SOFCs, the size dependence of materials catalytic properties and the overlaps in the characteristic time and spatial scales of electrode processes, further complicate the electrochemo-structural interactions, and make it difficult to analyze the electrode processes. Up to date, only a few reports are available on the structure-property relationships of the nano-structured electrodes. A widely-accepted mechanism has not been achieved. But several arguments have been proposed concerning the idealized understandings of the complex nano-structures. Zhu and co-workers [11] developed a geometric model for the nano-structured electrodes with the following idealizations: 1) the porous backbone network of electrode is considered to be a random packing system of spherical particles with a certain contacting angle to represent the degree of sintering, 2) the backbone is then covered by a monolayer of spherical nano-particles as the infiltrated catalytic material, 3) the rate-limiting reactions take place at the backbone/infiltrate/pore three-phase boundaries (TPBs). This model predicts that the nano-structured electrodes have a higher density of TPBs compared with the composite electrodes comprised of micron-sized particles by powder-mixing-sintering process, therefore indicating a lower electrode polarization resistance of nano-structured electrodes. Ding et al. [12] refined this model and suggested that a heavy infiltration loading leads to multi-layer stacking of nano-particles and further produces isolated pores, therefore decreasing the density of accessible TPBs. This model provides an explanation of the optimal infiltration loading corresponding to the lowest polarization resistance in terms of accessible TPB length. Another model is proposed by Tanner et al. [13] who idealized the electrode as regularly-spaced backbone slabs coated by a dense infiltrate thin film. The electrode polarization resistance is expressed as an explicit function of the width and the spacing of the slabs. This model proposed a conceptual design for the nano-structured electrodes before the surge of experimental studies. Nicholas et al. [14] developed a refined version of this model, considering that the backbone slabs are coated by the infiltrate as a monolayer of isolated, hemispherical nanoparticles, which is much closer to the true microstructures. Shah et al. [15] assumed that the electrode polarization resistance is dominated by surface area of the hemispherical infiltrate nanoparticles. These models are essentially of the zeroth-order. Compared with the models by Tanner, Nicholas and Shah, the models by Zhu and Ding seem more suitable in describing the electrode backbone, since the backbone is usually fabricated by sintering of granular powder slurry. In fact, the random-packed-sphere approach has been widely used in modeling composite electrodes [16-19]. One issue, however, is the need of careful calibrations of the contacting angle between backbone particles, which introduces additional uncertainties. Another issue is the controversy in assigning the contacting angle between infiltrated particles and backbone particles. Zhu and Ding assumed a contacting angle of 15° [11, 12], while Nicholas and Shah used 90° (hemispherical) [14, 15]. In terms of the structure-property relationship, the models by Zhu and Ding are applicable to the electrodes where surface exchange reactions are constricted at TPBs, e.g. (La,Sr)MnO_3 (LSM) infiltrated yttria-stabilized zirconia (YSZ) electrodes. The models by Tanner, Nicholas and Shah are usually applied to the electrodes where surface exchange reactions take place at the surface of infiltrated particles, e.g. $(La,Sr)(Co,Fe)O_3$ infiltrated electrodes. Although analytic, these models face challenges in making quantitative predictions due to over-simplifying the electrode microstructures. In addition, numerical simulations have been developed to simulate the true 3D nano-structured electrodes. Zhang et al.[20-22] studied the evolution of geometric properties of the electrodes, e.g. total and percolated TPB lengths, surface/interface areas, and tortuosity factors of single/dual-phase backbone infiltrated by single/dual-phase nanoparticles, as a function of infiltration loading with a numerical random-packed-sphere algorithm, considering the risk of aggregation of infiltrated nanoparticles. They also performed Monte Carlo simulations to study the coarsening of nanostructures [23]. Researchers have developed other models, such as the particle-based numerical models [24, 25] and the phase-field models [26, 27] for better understandings of infiltrated electrode microstructures in a general manner. However, the empirical model parameters need careful calibrations to represent true microstructures. Quantification of electrode microstructures is therefore critical to resolving the structure-property relationships. In the past decade, X-ray computed tomography (XCT) and focused ion beam serial sectioning- scanning electron microscopy (FIB-SEM) have been employed to image the 3D microstructures of SOFC electrodes [28-33]. According to the record of Web of Science database by searching topic on "solid oxide cell" & "tomography" or "FIB", more than 500 articles have been published since the first attempt of reconstructing a SOFC Ni-YSZ anode by FIB-SEM in 2006 [29]. Almost all studies were demonstrated on the composite electrodes prepared by powder-mixing and sintering processes, such as Ni-YSZ [34], LSM-YSZ [32, 33] and porous mixed-conducting perovskite electrodes [31], since the characteristic feature in the composite electrodes, such as the particle size (usually of micron or sub-micron), could be captured clearly by the state-of-the-art 3D imaging technologies with a typical resolution of 10-50 nm. For the reconstruction of nano-structured electrodes, however, only two attempts are reported by one research group, who utilized FIB-SEM to reconstruct Ni infiltrated YSZ anodes [35, 36]. There is not yet a report for reconstruction of nano-structured electrodes using XCT. Although extensive experimental studies have been performed on nano-structured electrodes, the 3D microstructures have not been well quantified. Therefore, more efforts are needed for correlation between electrode microstructures and properties in nano-structured electrodes.

In a previous work [37], a high-throughput 3D reconstruction method was developed based on a multi-stage recovering procedure of distance correlation functions (DCFs). This method provides a feasibility of reconstructing 3D microstructures from a single phase-segmented 2D micrograph at a micron-scale resolution. Since a nano-resolution 2D micrograph is easily obtainable by 2D imaging technologies, e.g. SEMs, the DCF recovering method is in principle applicable to reconstructing the nano-structured SOFC electrodes.

In this work, a 3D reconstruction of LSM infiltrated YSZ electrode from one representative nano-resolution (7.5 nm) 2D micrograph is demonstrated using the DCF recovering method. The geometric characteristics of electrodes under different LSM loadings are then calculated from the 3D reconstructions, and correlated quantitatively to the electrode performance by analyzing the distribution of relaxation times (DRT) of the impedance spectra. The ability of capturing nano-scale spatial features of the DCF recovering method is validated by a FIB-SEM dataset of a composite Ni-YSZ electrode with 50 nm resolution.

2. Experimental

2.1 Fabrication of Symmetric LSM infiltrated YSZ Cells

NiO powders, synthesized by a glycine-nitrate process were used as the pore former of the YSZ backbone to introduce uniformly sized and distributed pores. $Ni(NO_3)_2 \cdot 6H_2O$ ($\geq$ 98%, Sinopharm Chemical Reagent Co. Ltd) were dissolved in distilled water, and glycine was subsequently added to the solution with a molar ratio of glycine:Ni^{2+} as 0.6914:1. The solution was then heated on a hot plate until ignited to flame. Then the as-synthesized powders were calcined at 850 °C for 4 h. The YSZ ($Y_{0.16}Zr_{0.84}O_{2-\delta}$, Fuel Cell Materials) powders were uniaxially pressed into pellets under 250 MPa, with a 13 mm diameter stainless steel die. To prepare the porous YSZ frame of the electrode layers, YSZ and NiO powders with 60 wt.% NiO were mixed with ethyl cellulose and α-terpineol to obtain a YSZ-NiO slurry. Then, the slurry was printed symmetrically onto both sides of the fresh YSZ pellets via a screen-printing technique. After drying, the fresh sandwich bodies were sintered at 1450 °C for 5 h in air to obtain a NiO-YSZ/YSZ/NiO-YSZ three-layer structure. The pellets were then treated in H_2/Ar (5 % H_2) at 750 °C for 150 minutes to reduce NiO to Ni. The reduced samples were leached in a 2.0 M nitric acid solution at 90 °C for 12 h to remove Ni. Then, the porous YSZ backbones were infiltrated with 0.2 M LSM ($La_{0.8}Sr_{0.2}MnO_{3-\delta}$) solution, a mixture of $La(NO_3)_3 \cdot nH_2O$ ($\geq$99.0%), $Sr(NO_3)_2$ ($\geq$99.5%), $Mn(NO_3)_2$ ($\geq$99%) and glycine (Sinopharm Chemical Reagent Co. Ltd). The molar ratio of glycine to nitrate was 0.5. Each infiltration step was followed by drying and heating at 750 °C for 2 h to form LSM nanoparticles.

2.2 Electrochemical Characterization

Silver pastes (Sina-Platinum Metals Co. Ltd.) were applied on both sides of the symmetrical cells as the current collector. The electrochemical impedance spectra of the infiltrated symmetric cells at 600 - 850 °C in air were measured using an electrochemical workstation (Solartron 1260 & 1287) with an AC amplitude of 10 mA in the frequency range typically from 1 MHz to 0.01 Hz. DRT of electrochemical processes were calculated from the impedance spectra [38].

2.3 Collection of 2D micrographs and 3D reconstructions

Internal pores in electrodes were filled by immersing the symmetric cells in epoxy resin (EpoFix, Electron Microscopy Sciences, Hatfield, PA) for 10 min, and then hardened for 12 h in air. Each cell pellet was cut with a diamond saw to obtain two fracture surfaces with a crossing angle of about 100^{o}. Then the fracture surfaces were ground using SiC papers from 240 to 800 grit, and polished by colloidal silica (W0.25). FIB milling (HELIOS NanoLab 600i, FEI) was used to fabricate a 2D cross-section of the electrode, normal to one as-polished surface of the sample, as schematically demonstrated in Fig. 1. In order to enhance the contrast between LSM and YSZ, high-magnified (15000×) localized micrographs were collected using SEM InLens signal (ZEISS SUPRA55) with a voltage of 5 kV, and then stitched for each electrode. An anisotropic diffusion smoothing was applied on the raw SEM micrograph to eliminate noise. The phases of LSM, YSZ and pores were segmented using a watershed algorithm. Then, the 3D microstructure was reconstructed via a N-stage two-point exchanging process so that its DCFs converge to those of the 2D micrographs. Mathematically, the global objective is to minimize the energy functional, defined by,

$$\varepsilon = \frac{1}{\max(m)} \sum_{i,j,\mathbf{\Gamma},m} \left[\log_{10} DCF^{n}_{3\mathrm{D};i,j;\mathbf{\Gamma}}(m) - \log_{10} DCF^{N+1-n}_{2\mathrm{D};i,j;\mathbf{\Gamma}}(m) \right]^2 \qquad (1)$$

where $DCF^{N+1-n}_{2\mathrm{D};i,j;\mathbf{\Gamma}}(m) / DCF^{n}_{3\mathrm{D};i,j;\mathbf{\Gamma}}(m)$ denotes the DCFs between phase i and phase j of the 2D/3D microstructures at a distance of m pixels/voxels along direction $\mathbf{\Gamma}$ at the n^{th} stage of reconstruction. The direction $\mathbf{\Gamma}$ consists of nearest neighbor (NN) directions

([100], [010], [001]) and the next-nearest neighbor (NNN) directions ([110], $[1\bar{1}0]$, [101], $[10\bar{1}]$, [011], $[01\bar{1}]$). A detailed explanation of the DCF recovering method is reported in [37]. In this work, the two-point swap was accepted if the energy functional is decreased and the total TPB length of the 3D microstructure approaches to the TPB length of the 2D micrograph determined by the stereological method [39]. The exchanging process continued until ε was below 10^{-7}, or ε ceased deceasing after 100 continuous attempts of two-point swaps. Geometric characteristics of the 3D reconstructed microstructures were then calculated [21, 40].

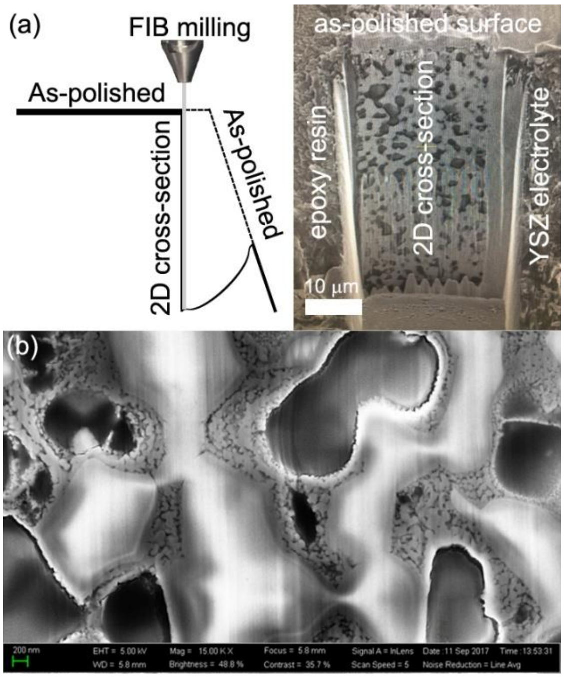

Figure 1. Schematic diagram showing the fabrication of 2D cross-section of the LSM infiltrated YSZ cathode by FIB milling (a) and a high-magnification image of the 2D cross-section collected by SEM InLens signal under low voltage (b).

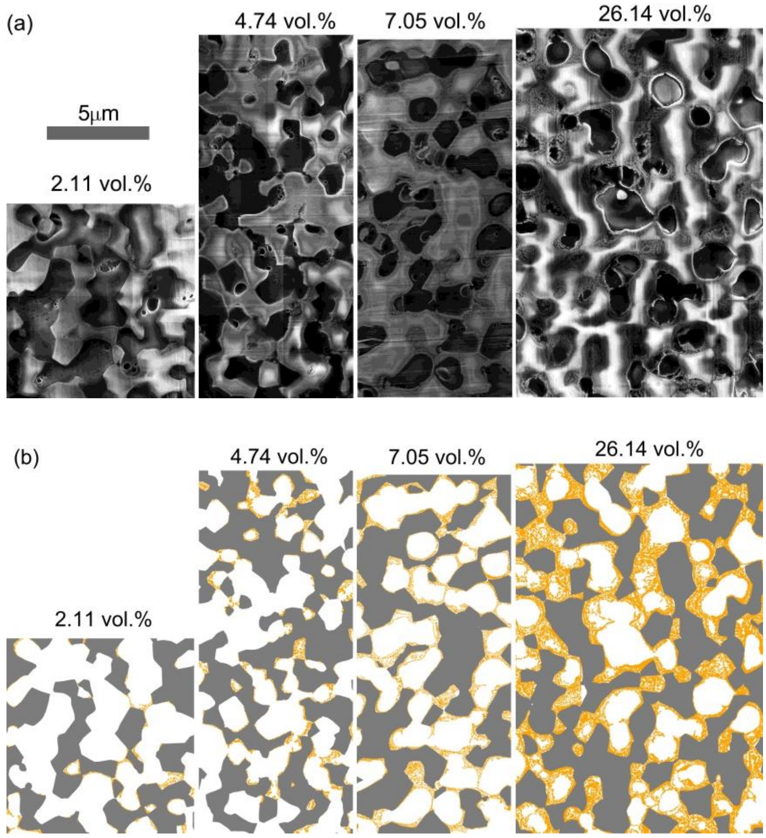

Figure 2. 2D cross-sectional micrographs of the LSM infiltrated YSZ electrodes with LSM loadings of 2.11, 4.74, 7.05 and 26.14 vol.%. a) SEM images of the electrodes, which are spliced from several SEM images to obtain a big field of view under a high resolution. b) Phase segmented images where yellow color denotes LSM, gray color denotes YSZ and white color denotes pores.

3. Results and discussion

Fig. 2 shows the raw SEM image (Fig.2a) and the phase-segmented micrographs (Fig. 2b) of the LSM infiltrated YSZ electrodes at various LSM loadings. The pixel size of the micrographs is 7.5 nm. According to the phase-segmented micrographs, LSM loadings for the electrodes are determined to be 2.11, 4.74, 7.05 and 26.14 vol.%. Then, the 3D microstructures at different LSM loadings are reconstructed based on the DCFs between LSM, YSZ and pore phases from the 2D phase-segmented micrographs. As is known, the effective thickness of composite SOFC electrodes is about 10 μm. For nano-structured electrodes, the effective thickness is relatively smaller [41]. Therefore, the target dimension of the 3D

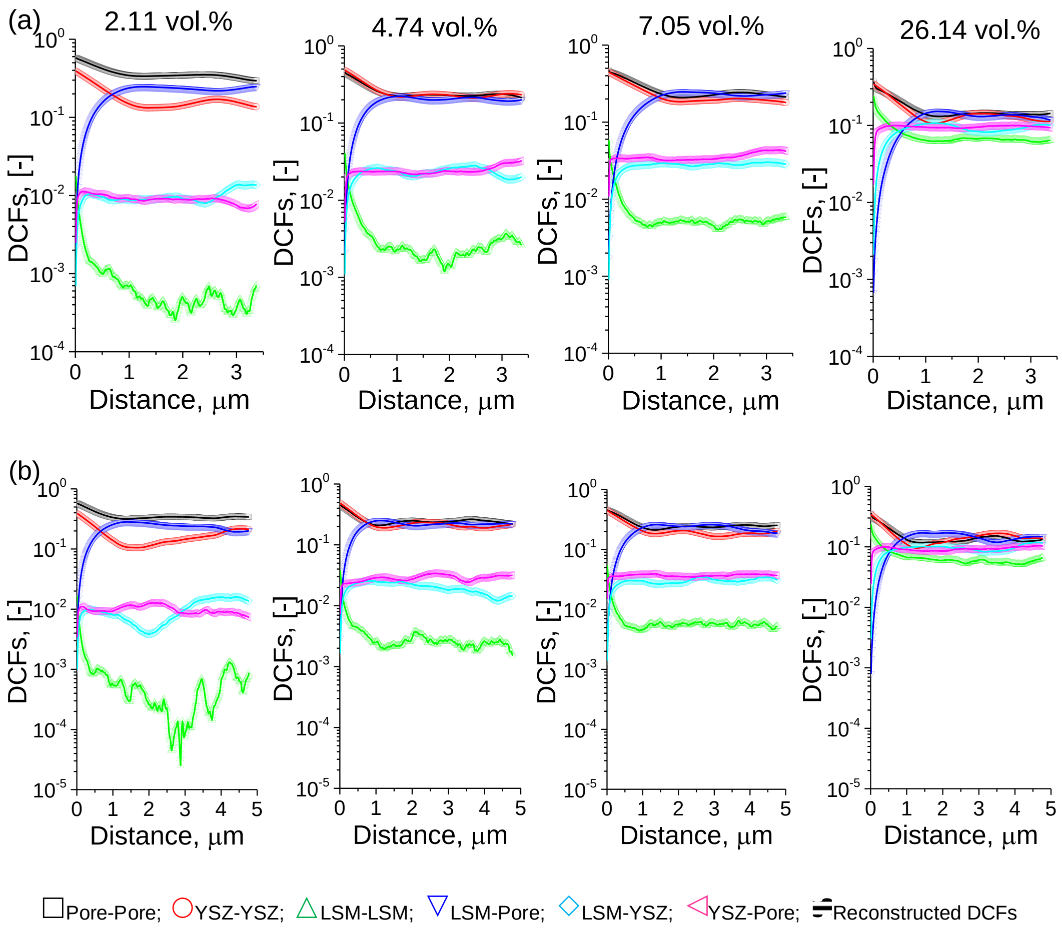

Figure 3. DCFs along NN (a) and NNN (b) directions of the binary pairs between LSM, YSZ and pores. Scatters denote the objective DCFs of the 2D micrographs shown in Fig. 2b. Lines denote the DCFs of the reconstructed electrodes.

reconstructed microstructures is set as 1024×1024×1024 voxels with a voxel size of 7.5 nm, that is 7.68×7.68×7.68 μm^3. This dimension is huge compared to those by other 3D imaging technologies (200 ~ 400 voxels in each dimension). To this end, a six-stage reconstruction is used. Due to the tremendous difference in the characteristic sizes of LSM and YSZ particles, the first four stages only reconstruct the YSZ backbone, and LSM infiltrate is then introduced at the end of the 4th stage by replacing pore voxels close to backbone with LSM voxels. The reconstructions of the four electrodes are accomplished within 60 hours, running on a custom-built

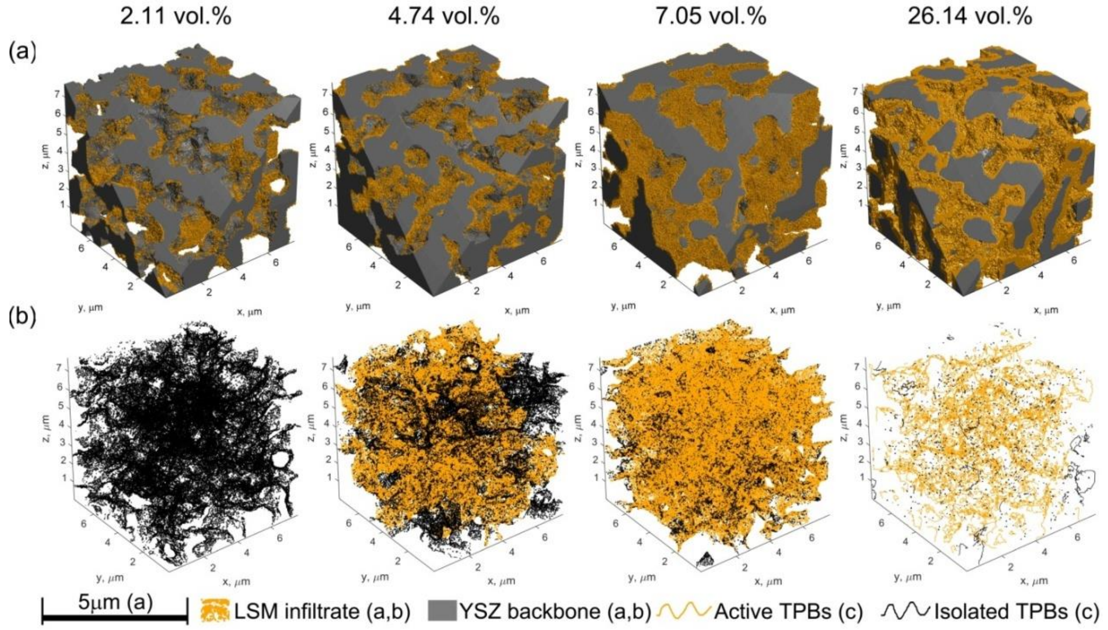

Figure 4. 3D reconstruction of the LSM infiltrated YSZ electrodes with several LSM loadings. a) 3D reconstructed microstructures with a dimension of 1024×1024×1024 voxels at a voxel size of 7.5 nm by the DCF method, according to the 2D micrographs in Fig. S6. A corner is cropped off for better visualization. b) 3D distributions of three-phase boundaries, calculated from the matrixes in (a).

workstation equipped with 128 GB RAM and 2.6 GHz CPU (32 cores). The DCFs of the reconstructed microstructures match with those of the 2D micrographs (Fig. 3). In particular, the DCFs with low values and tiny fluctuations for the nano-sized, low-content LSM infiltrate are captured accurately, due to the logarithmic DCFs in the criterion of energy functional (Eq. 1). The 3D reconstructed microstructures of the electrodes are shown in Fig. 4a (LSM in yellow, YSZ in gray, and pores transparent). Based on the 3D reconstructions, distributions of TPBs are calculated and visualized in Fig. 4b. Herein, TPBs are separated into isolated TPBs (in black) and active (or

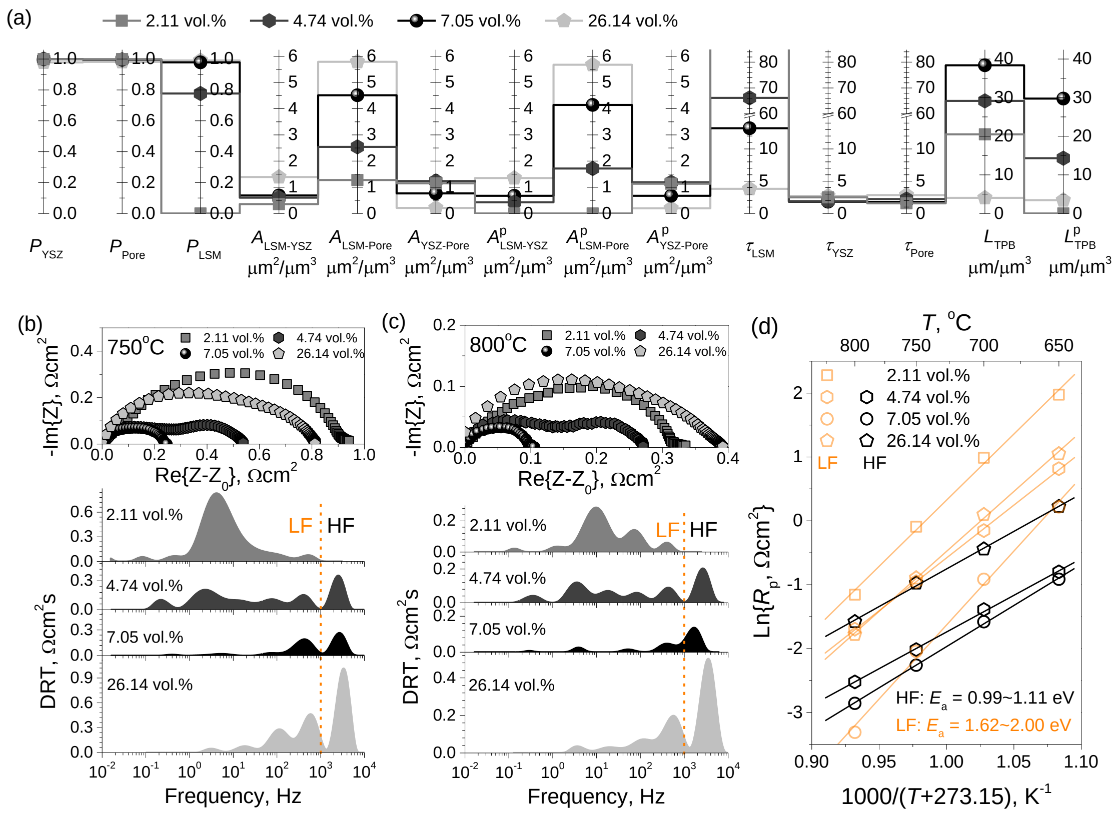

Figure 5. Quantitative analysis of the LSM infiltrated YSZ electrodes with the various LSM loadings. a) Geometric properties of the reconstructed electrodes. b, c) Electrochemical impedance of the electrodes measured in symmetric cells under open circuit condition and the distribution of relaxation times (DRT) at (b) 750 °C and (c) 800 °C. d) Temperature dependence of the polarization resistances (R_p) of the high frequency (HF) process and the low frequency (LF) process, determined from the DRT data shown in (b, c).

percolated) TPBs (in yellow). As shown in Fig. 4b, with 2.11 vol.% LSM, all TPBs are isolated. Active TPBs form at 4.74 vol.% LSM, and increase as the LSM content increase to 7.05 vol.%. However, active TPBs decrease dramatically when LSM content is 26.14 vol.%. The variation in TPBs with LSM content indicates a change in electrode performance. Fig. 5 shows the quantitative analysis of geometric properties (Fig. 5a), including percolation probabilities of YSZ (P_{YSZ}), Pore (P_{Pore}), LSM (P_{LSM}) networks, the total and percolated volumetric densities of LSM-YSZ interface ($A_{\mathrm{LSM\text{-}YSZ}}$, $A^{\mathrm{P}}_{\mathrm{LSM\text{-}YSZ}}$), LSM surface ($A_{\mathrm{LSM\text{-}Pore}}$, $A^{\mathrm{P}}_{\mathrm{LSM\text{-}Pore}}$), YSZ surface ($A_{\mathrm{YSZ\text{-}Pore}}$, $A^{\mathrm{P}}_{\mathrm{YSZ\text{-}Pore}}$), the tortuosity factors of LSM (τ_{LSM}), YSZ (τ_{YSZ}) and Pore (τ_{Pore}) networks, the total and active TPB length densities (L_{TPB}, $L^{\mathrm{P}}_{\mathrm{TPB}}$), and electrochemical impedance analysis of the electrodes (Fig. 5b-d). As shown in Fig. 5a, the percolation probabilities of YSZ (P_{YSZ}) and pores (P_{Pore}) are nearly 100%, independent of the LSM content. With 2.11 vol.% LSM loading, the percolation probability of LSM (P_{LSM}) is zero, leading to zero percolated LSM-YSZ interface area ($A^{\mathrm{P}}_{\mathrm{LSM\text{-}YSZ}}$), zero percolated LSM surface area ($A^{\mathrm{P}}_{\mathrm{LSM\text{-}Pore}}$), infinite LSM tortuosity factor (τ_{LSM}) and zero active TPB length ($L^{\mathrm{P}}_{\mathrm{TPB}}$). With the increase of LSM content, percolation probability of LSM increases, forming active TPBs. In addition, LSM-YSZ interface area increase when YSZ surface area decreases, thus leading to a maximum TPB length at 7.05 vol.% LSM. As indicated by the Nyquist plots of electrode impedance spectra in Fig. 5b and 5c, the electrode polarization resistance first decreases to a minimum as the LSM content increases to 7.05 vol.%, and then increases notably at 26.14 vol.% LSM. This trend agrees with the variation in TPB length. The other geometric factors, however, change monotonously or are insensitive to LSM loadings. Thus, TPB length is strongly correlated with electrode performance. A stronger evidence is shown by the plots of distribution of relaxation times (DRT) in Fig. 5b and 5c. The DRT at 2.11 vol.% LSM exhibits the feature of Gerischer impedance, which can be attributed to the co-limitation of adsorption and diffusion of oxygen species at the internal surface of the electrode[42]. In this case, LSM particles are isolated, and cannot provide

Table 1. Geometric properties resolved from the 3D reconstruction, polarization resistance of the high frequency process (charge transfer at TPBs) of the electrodes and ionic conductivity of YSZ for calculation of charge transfer resistance per TPB length. R_{HF} is the resistance of the HF process, σ_{YSZ} is the ionic conductivity of YSZ, ϕ_{YSZ} is the volume fraction of YSZ backbone, $L^{\mathrm{P}}_{\mathrm{TPB}}$ is the active TPB length density, and τ_{YSZ} is the tortuosity factor of YSZ backbone.

ϕ_{LSM}	ϕ_{YSZ}	τ_{YSZ}	$L^{\mathrm{P}}_{\mathrm{TPB}}$	R_{HF}, Ωcm^2			
vol.%	vol.%		μm^{-2}	650 °C	700 °C	750 °C	800°C
4.74	49	1.89	14.32	0.225	0.125	0.0666	0.0401
7.05	45	1.79	29.75	0.200	0.103	0.0522	0.0287
26.14	35	1.93	3.45	0.625	0.321	0.189	0.103
σ_{YSZ}, Scm^{-1}				9.05×10^{-3}	1.64×10^{-2}	2.68×10^{-2}	4.10×10^{-2}

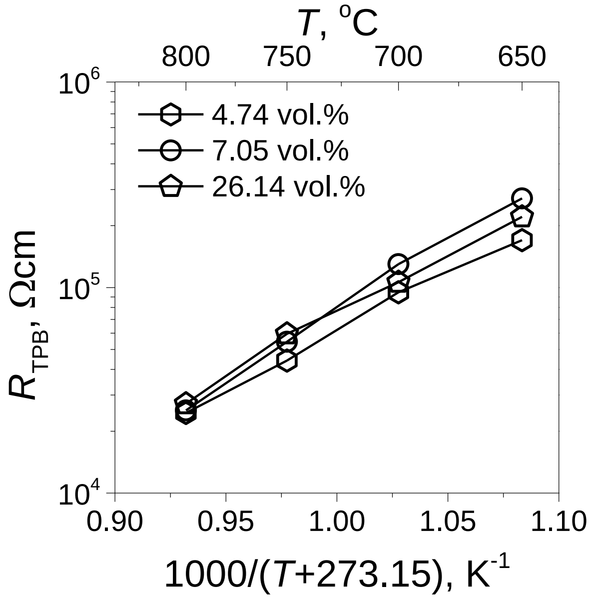

Figure 6. Temperature dependence of charge transfer resistance per TPB length (R_{TPB}), determined from the particle layer model and the data shown in Table 1.

electronic conduction, thereby restricting charge transfer reactions to the interface between current collector and electrode. At higher LSM loadings, a new DRT peak (or process) at high frequency (HF, 10^3-10^4 Hz) appears, while the Gerischer-like peak at low frequency (LF) are eclipsed, indicating a transition in reaction mechanisms. In this case, LSM particles are connected into percolated networks, thus active TPBs are connected throughout the electrode. It is noted that the variations in the resistance of the HF process (enclosed area by the peak) with respect to LSM loading coincide with the changes in the active TPB length. In addition, the temperature dependence of resistance (Fig. 5d) shows that the LF and HF peaks reflect different physical natures. Featured by the activation energy of 0.99-1.11 eV, the HF peak is attributed to the charge transfer process at active TPBs [43], where direct TPB reactions [44] and the reaction-diffusion process at the vicinity of TPBs [42] can be included. With the particle-layer model [41], we can resolve the charge transfer resistance per TPB length, given by

$$R_{\mathrm{TPB}} = R_{\mathrm{HF}}{}^{2}\sigma_{\mathrm{YSZ}}\phi_{\mathrm{YSZ}}L_{\mathrm{TPB}}^{\mathrm{P}} / \tau_{\mathrm{YSZ}} \tag{2}$$

where R_{HF} is the resistance of the HF process, σ_{YSZ} is the ionic conductivity of YSZ, and ϕ_{YSZ} is the volume fraction of YSZ backbone (Table 1). R_{TPB} of the electrodes are determined to be 2.5×10^4 Ωcm (800 °C), 5.5×10^4 Ωcm (750 °C), 1.1×10^5 Ωcm (700 °C) and 2.5×10^5 Ωcm (650 °C), which are insensitive to LSM content, or in other words insensitive to active TPB length, as shown in Fig. 6. Therefore, the electrode performance can be understood rationally by the 3D reconstruction results, demonstrating a new way of studying nanostructured electrodes.

The feasibility of the 3D reconstruction method for capturing nano-scale geometric features is verified using the FIB-SEM dataset of an isotropic porous Ni-

YSZ anode with a dimension of 256×256×256 voxels and a voxel size of 50 nm, as published in a previous work [34]. A four-stage reconstruction is performed and the

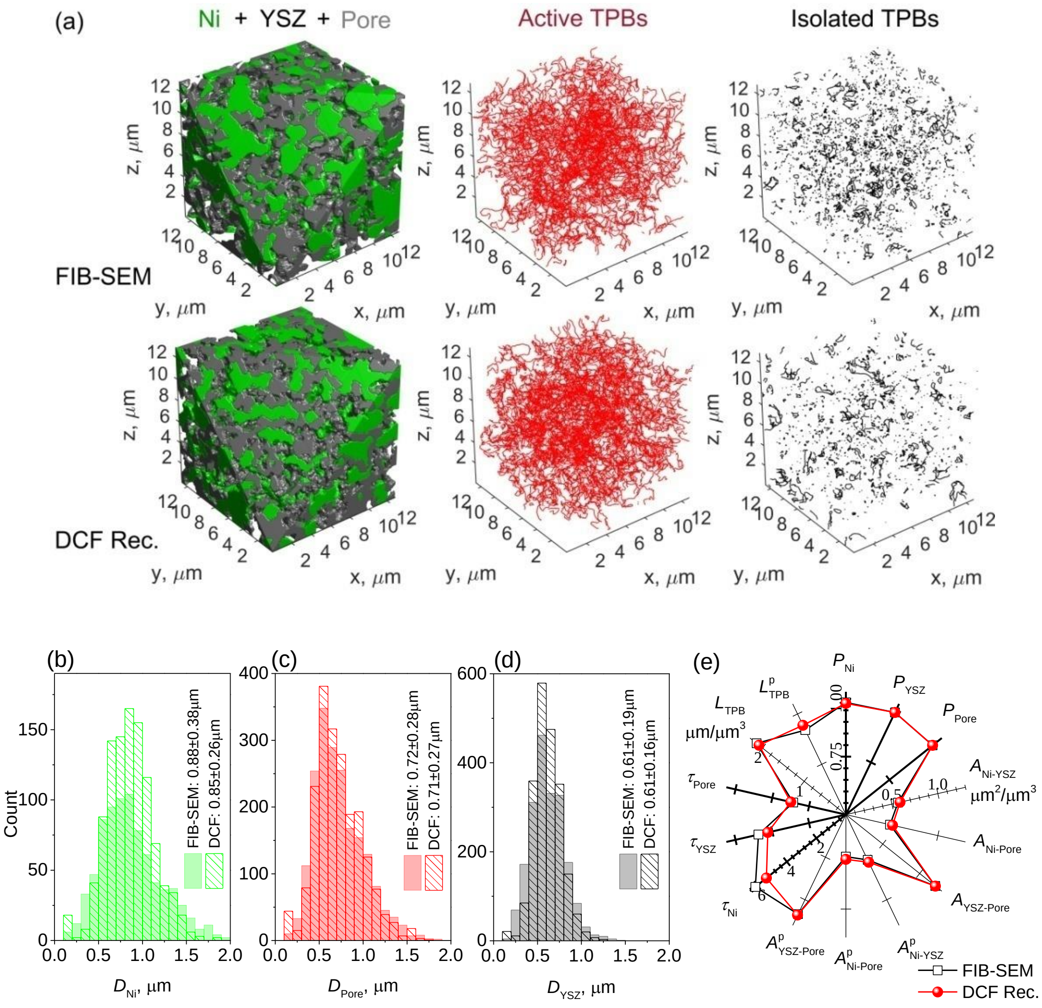

Figure 7. The 3D reconstructions by the DCF method and FIB-SEM of the porous Ni-YSZ anode functional layer. a) 3D visualization of the anode, the active TPBs and the isolated TPBs, by FIB-SEM and the DCF method. Spatial resolution is 50 nm. b-d) comparison of the distributions of (b) diameter of Ni (D_{Ni}), (c) pore (D_{Pore}) and (d) YSZ (D_{YSZ}). e) comparison of geometric factors, including the percolation probabilities of Ni (P_{Ni}), YSZ (P_{YSZ}), pore (P_{Pore}) networks, the internal area densities of Ni-YSZ interface ($A_{\mathrm{Ni\text{-}YSZ}}$), Ni surface ($A_{\mathrm{Ni\text{-}Pore}}$), YSZ surface ($A_{\mathrm{YSZ\text{-}Pore}}$), the percolated internal area densities ($A^{\mathrm{p}}_{\mathrm{Ni\text{-}YSZ,\ Ni\text{-}Pore,\ YSZ\text{-}Pore}}$), the tortuosity factors of Ni (τ_{Ni}), YSZ (τ_{YSZ}) and

pore (τ_{Pore}) networks, the three phase boundary length density (L_{TPB}), and the percolated three phase boundary length density ($L^{\mathrm{P}}_{\mathrm{TPB}}$).

objective DCFs are calculated from the 3D FIB-SEM dataset. Fig. 7a visualizes the FIB-SEM determined Ni-YSZ anode, the networks of Ni, YSZ and TPBs and the corresponding reconstructed results, showing that the reconstructed microstructure is not exactly a duplicate of the real microstructure. The DCFs are in nature reduce-dimension descriptors of microstructures, thus, cannot reproduce the real microstructure, but can generate a microstructure with the same statistical significance of geometric properties with the true microstructure. Fig. 7b-e show the key geometric properties, including particle diameter distributions of Ni (D_{Ni}), Pore (D_{Pore}) and YSZ (D_{YSZ}), percolation probabilities of Ni (P_{Ni}), YSZ (P_{YSZ}), pore (P_{Pore}) networks, the total and percolated volumetric densities of Ni-YSZ interface ($A_{\mathrm{Ni\text{-}YSZ}}$, $A^{\mathrm{P}}_{\mathrm{Ni\text{-}YSZ}}$), Ni surface ($A_{\mathrm{Ni\text{-}Pore}}$, $A^{\mathrm{P}}_{\mathrm{Ni\text{-}Pore}}$), YSZ surface ($A_{\mathrm{YSZ\text{-}Pore}}$, $A^{\mathrm{P}}_{\mathrm{YSZ\text{-}Pore}}$), the tortuosity factors of Ni (τ_{Ni}), YSZ (τ_{YSZ}) and pore (τ_{Pore}) networks, the total and active TPB length densities (L_{TPB}, $L^{\mathrm{P}}_{\mathrm{TPB}}$). It is shown that all the geometric properties of the reconstructed microstructure agree quantitatively with those of the FIB-SEM dataset.

4. Conclusions

Using the multi-stage DCF recovering method, the 3D microstructures of LSM infiltrated YSZ electrodes are reconstructed with 10^9 voxels from one 2D micrograph with super-resolution, which is easily obtainable by SEMs. The geometric parameters, such as the percolation probabilities and tortuosity factors of 3D interpenetrating networks, surface/interface areas, and TPB length are calculated from the 3D reconstructions, and studied systematically at various LSM infiltration loadings. The evolution of geometric properties is correlated quantitatively to the evolution of the characteristics of electrode impedance spectrum with the aid of DRT analysis. Our approach suggests an easy-to-use, high-throughput and super-resolution strategy of reconstructing 3D nano-structured SOFC electrodes and resolving the processing-structure-property relationship. The ability of capturing nano-scale spatial features is validated by the FIB-SEM dataset of a Ni-YSZ electrode at a nano-resolution. This approach is general for applications in SOFC electrodes and can readily be applied to other materials with heterogeneously nano-scale features.

Acknowledgments

We gratefully acknowledge the financial support from Natural Science Foundation of China (21673062, 51402066, 51371070) and China Postdoctoral Science Foundation funded project (2015M571411, 2016T90282, LBH-Z15061, LBH-TZ1607) and the U.S. Department of Energy SECA Core Technology Program (DE-FE0031670).

References

1. Y. Zhang, Y. Chen, Y. Lin, M. Yan, W. M. Harris, W. K. S. Chiu, M. Ni, F. Chen, Electrochemical fields within 3D reconstructed microstructures of mixed ionic and electronic conducting devices, J. Power Sources 331 (2016) 167-179.
2. S. Jiang, Nanoscale and nano-structured electrodes of solid oxide fuel cells by infiltration: Advances and challenges, Int. J. Hydrogen Energy 37 (2012) 449-470.
3. J.M. Vohs, R.J. Gorte, High-Performance SOFC Cathodes Prepared by Infiltration, Adv. Mater. 21 (2009) 943-956.

4. D. Ding, X. Li, S. Y. Lai, K. Gerdes, M. Liu, Enhancing SOFC cathode performance by surface modification through infiltration, Energy Environ. Sci. 7 (2009) 552-575.
5. M. Liu, M.E. Lynch, K. Blinn, F.M. Alamgir and Y. Choi, Rational SOFC material design: new advances and tools, Mater. Today 14 (2011) 534-546.
6. Y. Chen, Y. Chen, D. Ding, Y. Ding, Y. Choi, L. Zhang, S. Yoo, D. Chen, B. de Glee, H. Xu, Q. Lu, B. Zhao, G. Vardar, J. Wang, H. Bluhm, E. J. Crumlin, C. Yang, J. Liu, B. Yildiz, M. Liu, A robust and active hybrid catalyst for facile oxygen reduction in solid oxide fuel cells, Energy Environ. Sci. 10 (2017) 964-971.
7. J. Myung, D. Neagu, D. N. Miller, J. T. S. Irvine, Switching on electrocatalytic activity in solid oxide cells, Nature 537 (2016) 528.
8. D. Neagu, G. Tsekouras, D. N. Miller, H. Ménard, J. T. S. Irvine, In situ growth of nanoparticles through control of non-stoichiometry, Nat. Chem. 5 (2013) 916.
9. O. Kwon, S. Sengodan, K. Kim, G. Kim, H. Y. Jeong, J. Shin, Y.-W. Ju, J.W. Han, G. Kim, Exsolution trends and co-segregation aspects of self-grown catalyst nanoparticles in perovskites, Nat. Commun. 8 (2017) 15967.
10. Z. Du, H. Zhao, S. Yi, Q. Xia, Y. Gong, Y. Zhang, X. Cheng, Y. Li, L. Gu, K. Świerczek, High-performance anode material $Sr_2FeMo_{0.65}Ni_{0.35}O_{6-\delta}$ with in situ exsolved nanoparticle catalyst, ACS Nano 10 (2016) 8660-8669.
11. W. Zhu, D. Ding, C. Xia, Enhancement in Three-Phase Boundary of SOFC Electrodes by an Ion Impregnation Method: A Modeling Comparison, Electrochem. Solid-State Lett. 11 (2008) B83-B86.

12. D. Ding, W. Zhu, J. Gao, C. Xia, High performance electrolyte-coated anodes for low-temperature solid oxide fuel cells: Model and Experiments, J. Power Sources 179 (2008) 177-185.

13. C. W. Tanner, K. Fung, A. V. Virkar, The effect of porous composite electrode structure on solid oxide fuel cell performance: I. theoretical analysis, J. Electrochem. Soc. 144 (1997) 21-30.

14. J. D. Nicholas, L. Wang, A. V. Call, S. A. Barnett, Use of the Simple Infiltrated Microstructure Polarization Loss Estimation (SIMPLE) model to describe the performance of nano-composite solid oxide fuel cell cathodes, Phys. Chem. Chem. Phys. 14 (2012) 15379-15392.

15. M. Shah, J. D. Nicholas, S.A. Barnett, Prediction of infiltrated solid oxide fuel cell cathode polarization resistance, Electrochem. Commun. 11 (2009) 2-5.

16. Q. Cai, C. S. Adjiman, N. P. Brandon, Modelling the 3D microstructure and performance of solid oxide fuel cell electrodes: Computational parameters, Electrochim. Acta 56 (2011) 5804-5814.

17. B. Kenney, M. Valdmanis, C. Baker, J. G. Pharoah, K. Karan, Computation of TPB length, surface area and pore size from numerical reconstruction of composite solid oxide fuel cell electrodes, J. Power Sources 189(2009) 1051-1059.

18. C. Metcalfe, O. Kesler, T. Rivard, F. Gitzhofer, N. Abatzoglou, Connected Three-Phase Boundary Length Evaluation in Modeled Sintered Composite Solid Oxide Fuel Cell Electrodes, J. Electrochem. Soc. 157 (2010) B1326-B1335.

19. A. Abbaspour, J.-L. Luo, K. Nandakumar, Three-dimensional random resistor-network model for solid oxide fuel cell composite electrodes, Electrochim. Acta 55 (2010) 3944-3950.

20. Y. Zhang, M. Ni, C. Xia, Microstructural insights into dual-phase infiltrated solid oxide fuel cell electrodes, J. Electrochem. Soc. 160 (2013) F834-F839.

21. Y. Zhang, Q. Sun, C. Xia, M. Ni, Geometric Properties of Nanostructured Solid Oxide Fuel Cell Electrodes, J. Electrochem. Soc. 160 (2013) F278-F289.

22. S. Wan, M. Yan, Y. Zhang, A numerical study of infiltrated solid oxide fuel cell electrode with dual-phase backbone, Int. J. Energy Res. 0 (2018).

23. Y. Zhang, M. Ni, M. Yan, F. Chen, Thermal aging stability of infiltrated solid oxide fuel cell electrode microstructures: A three-dimensional kinetic Monte Carlo simulation, J. Power Sources 299 (2015) 578-586.

24. P. Vijay, M. O. Tadé, Z. Shao, M. Ni, Modelling the triple phase boundary length in infiltrated SOFC electrodes, Int. J. Hydrogen Energy 42(2017) 28836-28851.

25. A. Bertei, J. G. Pharoah, D. A. W. Gawel, C. Nicolella, A Particle-Based Model for Effective Properties in Infiltrated Solid Oxide Fuel Cell Electrodes, J. Electrochem. Soc. 161(2014) F1243-F1253.

26. R. Davis, M. Haataja, Microstructural stability of supported metal catalysts: A phase field approach, J. Power Sources 369 (2017) 111-121.

27. L. Liang, Q. Li, J. Hu, S. Lee, K. Gerdes, L.-Q. Chen, Phase field modeling of microstructure evolution of electrocatalyst-infiltrated solid oxide fuel cell cathodes, J. Appl. Phys. 117(2015) 065105.

28. A. P. Cocco, G. J. Nelson, W. M. Harris, A. Nakajo, T. D. Myles, A. M. Kiss, J. J. Lombardo, W. K. S. Chiu, Three-dimensional microstructural imaging

methods for energy materials, Phys. Chem. Chem. Phys. 15 (2013) 16377-16407.

29. J. R. Wilson, W. Kobsiriphat, R. Mendoza, H. -Y. Chen, J. M. Hiller, D. J. Miller, K. Thornton, P.W. Voorhees, S.B. Adler, S.A. Barnett, Three-dimensional reconstruction of a solid-oxide fuel-cell anode, Nat. Mater. 5 (2006) 541.

30. K. N. Grew, Y. S. Chu, J. Yi, A. A. Peracchio, J. R. Izzo, Y. Hwu, F. De Carlo, W. K. S. Chiu, Nondestructive nanoscale 3D elemental mapping and analysis of a solid oxide fuel cell anode, J. Electrochem. Soc. 157 (2010) B783-B792.

31. Y. Lin, S. Fang, D. Su, K.S. Brinkman, F. Chen, Enhancing grain boundary ionic conductivity in mixed ionic-electronic conductors, Nat. Commun. 6 (2014) 6824.

32. G. Brunello, W. Epting, J. Silva, P. Salvador, S. Litster, H. Finklea, Y. Lee, K. Gerdes, D. Mebane, Quantitative interpretation of impedance spectroscopy data on porous LSM electrodes using X-ray computed tomography and Bayesian model-based analysis, Phys. Chem. Chem. Phys. 19 (2017) 25334-25345.

33. W. Epting, Z. Mansley, D. Menasche, P. Kenesei, R. Suter, K. Gerdes, S. Litster, P. Salvador, Quantifying intermediate frequency heterogeneities of SOFC electrodes using X-ray computed tomography, J. Am. Ceram. Soc. 100 (2017) 2232-2242.

34. Z. Jiao, N. Shikazono, 3D reconstruction size effect on the quantification of solid oxide fuel cell nickel-yttria-stabilized-zirconia anode microstructural information using scanning electron microscopy-focused ion beam technique, Sci. Bull. 61(2016) 1317-1323.

35. M. Kishimoto, M. Lomberg, E. Ruiz-Trejo, N.P. Brandon, Enhanced triple-phase boundary density in infiltrated electrodes for solid oxide fuel cells demonstrated by high-resolution tomography, J. Power Sources 266 (2014) 291-295.

36. A. Bertei, E. Ruiz-Trejo, K. Kareh, V. Yufit, X. Wang, F. Tariq, N. P. Brandon, The fractal nature of the three-phase boundary: A heuristic approach to the degradation of nanostructured solid oxide fuel cell anodes, Nano Energy 38 (2017) 526–536.

37. Y. Zhang, M. Yan, Y. Wan, Z. Jiao, Y. Chen, F. Chen, C. Xia, M. Ni, High-throughput 3D reconstruction of stochastic heterogeneous microstructures in energy storage materials, npj Comput. Mater. 5 (2019) 11.

38. Y. Zhang, Y. Chen, M. Yan, F. Chen, Reconstruction of relaxation time distribution from linear electrochemical impedance spectroscopy, J. Power Sources 283(2015) 464-477.

39. Y. Zhang, J. Ma, M. Yan, Is 2D stereological method good enough for quantification of solid oxide fuel cell electrode microstructure?, Sci. Bull. 61 (2016) 1313-1316.

40. Y. Zhang, C. Xia, M. Ni, Simulation of sintering kinetics and microstructure evolution of composite solid oxide fuel cells electrodes, Int. J. Hydrogen Energy 37(2012) 3392-3402.

41. Y. Zhang, C. Xia, A particle-layer model for solid-oxide-full-cell cathodes with different structures, J. Power Sources 195 (2010) 4206-4212.

42. S. B. Adler, Factors governing oxygen reduction in solid oxide fuel cell cathodes, Chem. Rev. 104 (2004) 4791-4844.

43. Y. Chen, Y. Bu, Y. Zhang, R. Yan, D. Ding, B. Zhao, S. Yoo, D. Dang, R. Hu, C. Yang, M. C. Liu, A highly efficient and robust nanofiber cathode for solid oxide fuel cells, Adv. Energy Mater. 7 (2017) 1601890.

44. M. Liu, Equivalent Circuit Approximation to Porous Mixed-Conducting Oxygen Electrodes in Solid-State Cells, J. Electrochem. Soc. 145 (1998) 142-154.